

DNS of Laminar-Turbulent Transition in a 3-D Aerodynamics Boundary-Layer Flow

P. Wassermann, M. Kloker

Institut für Aerodynamik und Gasdynamik,
Universität Stuttgart, Pfaffenwaldring 21, D-70550 Stuttgart, Germany

Abstract. Controlled laminar-turbulent transition of a 3-D boundary-layer flow caused by localized surface nonuniformities is investigated by means of spatial direct numerical simulations (DNS) based on the complete incompressible 3-D Navier-Stokes equations and a combined 6th-order compact Finite-Difference / spanwise Fourier-spectral scheme. The considered laminar spanwise-invariant flat-plate base flow is a model of the boundary-layer flow in the front region of a swept wing, with favorable and ensuing adverse chordwise pressure gradient. The primary downstream growth and nonlinear interaction of vortex-packet modes as well as the appearance of a secondary instability mechanism leading to turbulence is investigated in detail. The effectiveness of a steady, nonlinear, upstream flow deformation of the base flow with respect to significant transition delay is shown.

1 Introduction

On a swept-back airfoil the chordwise acceleration of the potential flow induces an inboard-oriented crossflow component inside the boundary layer

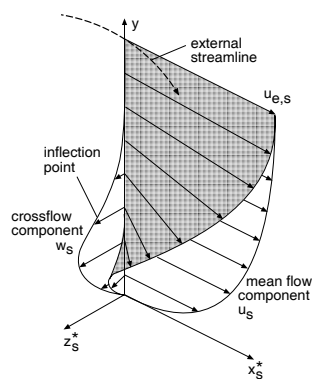


Fig. 1. 3-D boundary-layer velocity profile

perpendicular to the meanflow direction (Fig. 1). The crossflow velocity profile $w_s(y)$, y being the wall-normal coordinate, is inflectional and causes a strong primary instability of the flow with respect to so-called crossflow (CF) modes. The wave number vectors of both instationary and stationary CF modes - the latter referred to as CF vortices (CFVs) - are oriented approximately parallel to the crossflow direction. At low freestream-turbulence conditions, CFVs excited even by minute surface nonuniformity or roughness are found to be dominant (see e.g. [1] and [8] for experimental, and [2] for numerical evidence). Upon downstream vortex saturation, steady local inflectional streamwise velocity profiles $u_s(y)$ are formed and strong subsequent (secondary) instability mechanisms that are not yet fully understood typically lead to transition.

Up to date the bulk part of the research work has been devoted to laminar breakdown induced by a single saturated CF vortex mode in Falkner-Skan-Cooke similarity boundary-layer flows with constant Hartree parameter (see

[1]-[4] and [13]). Our present investigations focus on laminar breakdown induced by packets of disturbance modes rather than by individual modes in a more realistic base flow. Using mode packets the disturbance spectrum is richer, and the 3-D mean flow distortion induced by the steady CFV packet can be larger compared to a single vortex mode. Consequently, the secondary instability can set in stronger or earlier. First detailed investigations on packets of vortex modes as generated by localized surface disturbances are discussed in [11] and [12]. In this paper, a packet consisting of four CFV modes has been chosen as primary disturbance, and to trigger final breakdown, periodic background disturbance pulses or a monofrequent CF wave packet have been superimposed.

2 Governing Equations and Numerical Method

The numerical model is based on the complete 3-D Navier-Stokes equations for incompressible unsteady flows in a vorticity-velocity formulation. All variables are nondimensionalized by the reference length $\bar{L} = 0.05m$, the freestream velocity $\bar{U}_\infty = 30m/s$ and the Reynolds number $Re = \bar{U}_\infty \bar{L} / \bar{\nu} = 100000$, where $\bar{\cdot}$ denotes dimensional variables and $\bar{\nu}$ is the kinematic viscosity:

$$x = \bar{x} / \bar{L}, \quad y = \sqrt{Re} \cdot \bar{y} / \bar{L}, \quad z = \bar{z} / \bar{L}, \quad t = \bar{t} \cdot \bar{U}_\infty / \bar{L}, \quad (1)$$

$$u = \bar{u} / \bar{U}_\infty, \quad v = \sqrt{Re} \cdot \bar{v} / \bar{U}_\infty, \quad w = \bar{w} / \bar{U}_\infty \quad .$$

With the vectors of vorticity $\boldsymbol{\omega} = \{\omega_x, \omega_y, \omega_z\}^T$ and velocity $\mathbf{u} = \{u, v, w\}^T$, where u denotes the velocity in chordwise (x -), v in wall-normal (y -) and w in spanwise (z -) direction, the equations are:

$$\frac{\partial \omega_x}{\partial t} + \frac{\partial}{\partial y}(v\omega_x - u\omega_y) - \frac{\partial}{\partial z}(u\omega_z - w\omega_x) = \tilde{\Delta}\omega_x, \quad (2)$$

$$\frac{\partial \omega_y}{\partial t} - \frac{\partial}{\partial x}(v\omega_x - u\omega_y) + \frac{\partial}{\partial z}(w\omega_y - v\omega_z) = \tilde{\Delta}\omega_y, \quad (3)$$

$$\frac{\partial \omega_z}{\partial t} + \frac{\partial}{\partial x}(u\omega_z - w\omega_x) - \frac{\partial}{\partial y}(w\omega_y - v\omega_z) = \tilde{\Delta}\omega_z, \quad (4)$$

$$\frac{\partial^2 u}{\partial x^2} + \frac{\partial^2 u}{\partial z^2} = -\frac{\partial \omega_y}{\partial z} - \frac{\partial^2 v}{\partial x \partial y}, \quad (5)$$

$$\tilde{\Delta}v = \frac{\partial \omega_x}{\partial z} - \frac{\partial \omega_z}{\partial x}, \quad (6)$$

$$\frac{\partial^2 w}{\partial x^2} + \frac{\partial^2 w}{\partial z^2} = \frac{\partial \omega_y}{\partial x} - \frac{\partial^2 v}{\partial y \partial z}, \quad (7)$$

where $\tilde{\Delta}$ denotes the modified Laplace operator

$$\tilde{\Delta} = \frac{1}{Re} \frac{\partial^2}{\partial x^2} + \frac{\partial^2}{\partial y^2} + \frac{1}{Re} \frac{\partial^2}{\partial z^2} \quad . \quad (8)$$

The three vorticity components are defined as

$$\omega_x = \frac{1}{Re} \frac{\partial v}{\partial z} - \frac{\partial w}{\partial y}, \quad \omega_y = \frac{\partial w}{\partial x} - \frac{\partial u}{\partial z}, \quad \omega_z = \frac{\partial u}{\partial y} - \frac{1}{Re} \frac{\partial v}{\partial x}, \quad (9)$$

and at the wall the following equations are used:

$$\frac{\partial^2 \omega_x}{\partial x^2} + \frac{\partial^2 \omega_x}{\partial z^2} = -\frac{\partial^2 \omega_y}{\partial x \partial y} + \frac{\partial}{\partial z} \tilde{\Delta} v, \quad (10)$$

$$\frac{\partial \omega_z}{\partial x} = \frac{\partial \omega_x}{\partial z} - \tilde{\Delta} v. \quad (11)$$

We use a disturbance formulation, i.e. each flow variable is split into the steady 3-D base flow part (index B) and the unsteady 3-D disturbance flow part (denoted by a prime, note that for nonlinear disturbances the time mean $\langle f' \rangle \neq 0$):

$$f = f_B + f' \quad \text{with} \quad f \in \{u, v, w, \omega_x, \omega_y, \omega_z\}. \quad (12)$$

The simulation is carried out in a rectangular integration domain (Fig. 2). First, the steady base flow is calculated; subsequently, defined disturbances are introduced in a disturbance strip at the wall and the unsteady disturbance flow is calculated.

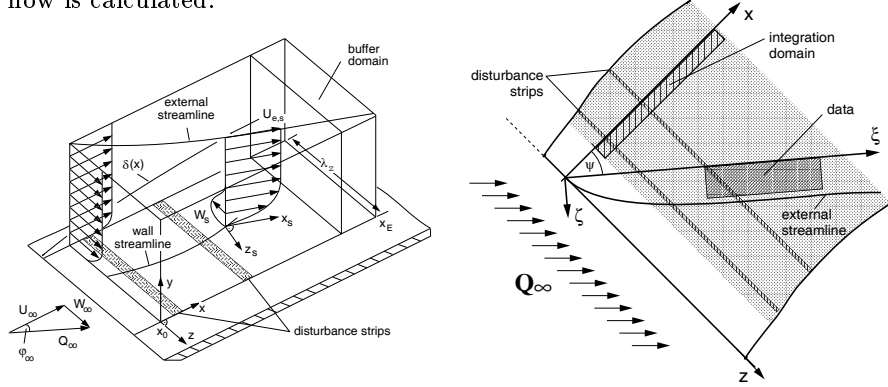


Fig. 2. Integration box with disturbance strips and 3-D velocity profiles (left) and top view of the swept flat plate (right) with the vortex-oriented coordinate system $((\xi, \zeta)$, rotated by $\psi = 39^\circ$ versus the chordwise system).

2.1 Calculation of the base flow

The calculation of the 3-D base flow relies strongly on the assumption of infinite span, i.e. all quantities are independent of the spanwise coordinate z , but there is a velocity component w_B in spanwise direction. The equations are obtained from (2)-(7) by neglecting all z -derivatives and are treated by

high-order finite differencing. The vorticity equations are solved by a semi-implicit pseudo-temporal technique, and the Poisson equations by a vectorizable stripe-pattern LSOR-technique (iteratively in x -direction).

The boundary conditions are no-slip condition at the wall and vanishing vorticity and a prescribed chordwise velocity distribution $u_e(x)$ at the upper boundary. At the outflow boundary the equations are solved by neglecting the second x -derivative or $1/Re$ terms following usual boundary-layer-theory assumptions, and u_B and w_B are calculated from

$$\frac{\partial^2 u_B}{\partial y^2} = \frac{\partial \omega_{z,B}}{\partial y} \quad , \quad \frac{\partial^2 w_B}{\partial y^2} = -\frac{\partial \omega_{x,B}}{\partial y}. \quad (13)$$

In this work, $u_e(x)$ at the upper boundary is gained from the potential velocity distribution $u_{p0}(x)$, valid at $y = 0$ in inviscid flow, by a complex flow function for potential flow. This function is obtained by integrating the analytical distribution $u_{p0}(x)$ (see section 3.1). Thus, an effect of the integration-domain height on the actual $u_\delta(x)$ ($\approx u_{p0}(x)$) and integral boundary-layer parameters is excluded. At the inflow boundary a local Falkner-Skan-Cooke solution appropriate to the local $u_e(x)$ is used.

2.2 Calculation of the disturbance flow

The equations for the disturbance quantities are derived from the equations (2)-(7) with the decomposition (12) leaving out the zero sum of all pure base-flow terms.

In spanwise direction the numerical method uses a complex Fourier spectral representation (the assumption of infinite span yields periodic boundary conditions) to calculate the nonsymmetric 3-D flow, i.e all variables are decomposed as

$$f'(x, y, z, t) = \sum_{k=-K}^K \hat{f}_k(x, y, t) \cdot e^{ik\gamma z}, \quad \hat{f}_k \in \mathbf{C}, \quad (14)$$

where γ is the basic spanwise wavenumber, related to the width λ_z of the integration domain by $\lambda_z = 2\pi/\gamma$. The \hat{f}_{-k} are the complex conjugates of the \hat{f}_k and do not have to be computed, but for \hat{f}_k both the real and imaginary parts of the equations have to be solved thus doubling the computational effort compared to a 3-D symmetric flow field. In x - and y -direction, a Finite-Difference (FD) discretisation is used, based on a blockwise equidistant rectangular grid with a special wall zone, where the stepsize Δy is halved. Principally, sixth-order compact FDs are used. The nonlinear terms in the vorticity transport equations are computed pseudospectrally and their x -derivatives are differenced with a special split-type method with inherent damping (see [6]); the time integration is done by a 4-step fourth-order Runge-Kutta (RK) method.

The boundary conditions at the upper boundary are vanishing vorticity and exponential decay or zero wall-normal derivative of the wall-normal velocity v' . At the inflow boundary all disturbance quantities are set to zero and at the wall the no-slip condition is satisfied for u' and w' . Also the velocity v' is zero at the wall, except in the disturbance strip, where the disturbances are forced, with momentum input but no net mass flow:

$$v'(x, y, z, t) = f_v(x) \cdot \left(\sum_{k=1}^K 2 \cdot A_{0,k} \cdot \cos(k\gamma z + \Theta_{0,k}) + \sum_{h=1}^H \sum_{k=-K}^K 2 \cdot A_{h,k} \cdot \cos(k\gamma z - h\beta t + \Theta_{h,k}) \right). \quad (15)$$

As for the outflow boundary, a well tested buffer-domain technique is applied, wherein the vorticity disturbance vector is ramped to zero upstream of the outflow boundary. A more detailed description of the numerical method is given in [2], [11] and for the main FD stencils see [6].

2.3 Computational aspects

The spanwise Fourier ansatz principally reduces the 3-D problem in physical space to a set of $(K+1)$ complex 2-D problems in Fourier space thus enabling a largely parallel computation in Fourier space. However, the modes are coupled by the nonlinear convective terms of the vorticity transport equations and are transformed to physical space ("pseudospectral method" with de-aliasing procedure) for the calculation of the nonlinear vorticity terms, which in turn are parallelized in streamwise direction.

The uniform equidistant grid contains maximal $2106 \times 257 \times 49 \cdot 73$ ($K=16-24$, 33 points in the wall zone) points in (x, y, z) -directions. The problem has been run on the supercomputers of the hww GmbH, Stuttgart, the NEC SX-4/32 (32 processors, 8 GB RAM) and the NEC SX-5 (16 processors, 32 GB RAM). As for the $K=16$ problem on the NEC SX-4 (2.6 GB memory requirement plus up to 1 GB XMU memory), the serial code reached ≈ 1 GFLOPS (of 2 GFLOPS theoretical peak performance) at a vector operation ratio of 99% and an average vector length of 190 after adapting the code to the specific features of the NEC SX-4. This results in a computation time of $3.6 \mu\text{s}$ per gridpoint and time step and a memory requirement of about 156 Byte per point. The NEC SX-4 parallel version reached a speed-up of 7 to 8 when computing on 9 processors parallel (two spectral modes per CPU) in everyday operation. The performance, however, depends heavily on the load of the computer. About 90% of the overall time was spent in parallel execution and only 10% of the total computation time for I/O, system-calls and serial program parts. The latest results have been calculated on the NEC SX-5 with a speedup of 1.7 per CPU compared to the NEC SX-4.

It is noted that the y -discretisation, especially in the near wall region, is the crucial point in resolution requirements. In the simulations presented here, the grid spacing was $\Delta x=0.00179$, $\Delta y=0.088$ ($\Delta y=0.044$ for the first 33 points, also recall the \sqrt{Re} -stretching) and $\Delta z=0.00191 - 0.00285$. The number of time steps per fundamental disturbance period ($\beta = 2\pi\bar{f}\bar{L}/\bar{U}_\infty = 20$) was 800. In the case with multi-frequent background disturbances the inflow boundary has been shifted downstream to $x = 1.68$, using (unsteady β - γ -Fourier component) boundary conditions in the second run at the inflow boundary extracted from the first computation within the domain; thus the number of grid points in x -direction is nearly halved.

3 Numerical Results

3.1 Base flow

The base flow is designed to resemble the flow in the front region of a swept wing. The streamwise edge velocity is defined analytically (see [10]) by

$$u_{p0}(x) = \frac{3}{2\pi} \left(\arctan\left(\frac{x-a}{b}\right) + \arctan\left(\frac{x+a}{b}\right) \right) - cx \quad (16)$$

$$\text{with } a = 0.2611, \quad b = 0.41015, \quad c = 0.056.$$

The integration domain starts at $x_0 = 0.25$ close to the leading edge (local Hartree $\beta_H(x_0) = 0.99$) and extends over a large distance downstream (outflow boundary at $x_E = 4.96$, for the following investigations the integration domain ends at $x_{ER} = 4.03$). The sweep angle is $\varphi_\infty = 45^\circ$ and the local

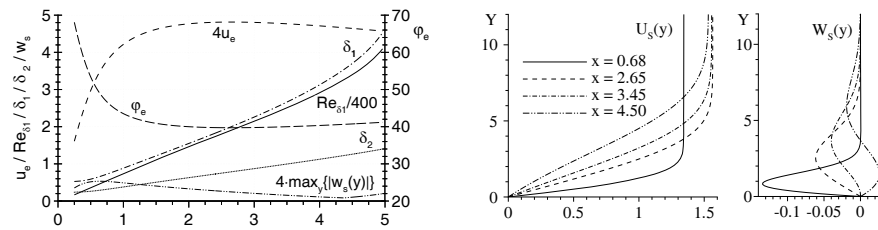


Fig. 3. Left: Base flow parameters. Right: Meanflow and crossflow profiles at various downstream positions.

angle of the external streamline varies from $\varphi_e(x_0) = 68.1^\circ$ to the minimum value of $\varphi_e = 39.7^\circ$ at $x = 2.65$ and $\varphi_e(x_E) = 41.1^\circ$. The Reynolds number based on the chordwise displacement thickness δ_1 rises from $Re_{\delta_1}(x_0) = 67$ to $Re_{\delta_1}(x_{ER}) = 1180$ and the displacement thickness increases by a factor of six within the domain. The maximum crossflow amplitude \bar{w}_s/\bar{U}_∞ is 13.3%, and for $x \geq 3.5$ the crossflow profiles $w_{B,s}(y)$ are S-shaped (see Fig. 3).

3.2 Primary Growth and Nonlinear Saturation of the CFV Packet

At first, the base flow has been analysed by means of spatial linear stability theory (LST) to get an overview of relevant instability modes. As a result, $\gamma_1 = 45$ ($= \bar{\gamma}_1 \cdot \bar{L}$) has been chosen for the subsequent DNS and the packet of the steady modes $(0, k)$, $k = 1-4$ has been introduced in the disturbance simulation by imposing a steady wall-normal velocity within the disturbance strip at the wall. The discrete waves are presented in the frequency-spanwise wavenumber spectrum (h, k) , so the mode $(0, k)$ denotes a stationary mode with the spanwise wavenumber $k \cdot \gamma_1$.

For the calculation of a nonlinearly saturated CFV scenario the CFV packet is introduced at $x_2 = 0.68$ with an amplitude of $A_{(0, k)} = 5.0 \cdot 10^{-3} \cdot \sqrt{Re}$. The spanwise phase of each mode is chosen in order to model a point-like perturbation (local "blowing" with momentum, but no net-mass-flow input, see Fig. 4). The disturbance components are strongly amplified first by primary instability and saturate at $x \approx 2.8$ with different amplitudes (Fig. 4).

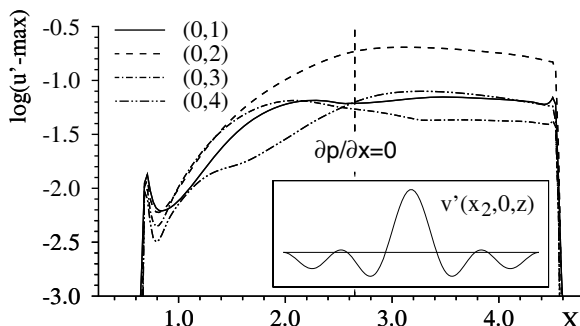


Fig. 4. Downstream $(t-z)$ -modal amplitude development (u' -maximum over y) of the CFV packet. Inset: forcing v' -velocity distribution in the x -center of the disturbance strip.

The mode $(0,2)$ attains the highest amplitude and clearly dominates by suppressing the modes $(0,1)$ and $(0,3)$. Accordingly, two streamwise, clockwise rotating vortices (when looking downstream) per spanwise wavelength are generated; one of them is stronger and further away from the wall (see Fig. 5, $\zeta \approx 0.0, 0.11, 0.22$). Note that the basic crossflow is in negative ζ -direction. Thus, slow fluid from the near wall region is brought up into faster regions resulting in a strong, steady deformation of the meanflow profiles $u_s(y)$ with relatively large y - and z -gradients. In Fig. 6 the vortices are visualized by means of LIC (Line Integral Convolution) in the same crosscut. In the upper

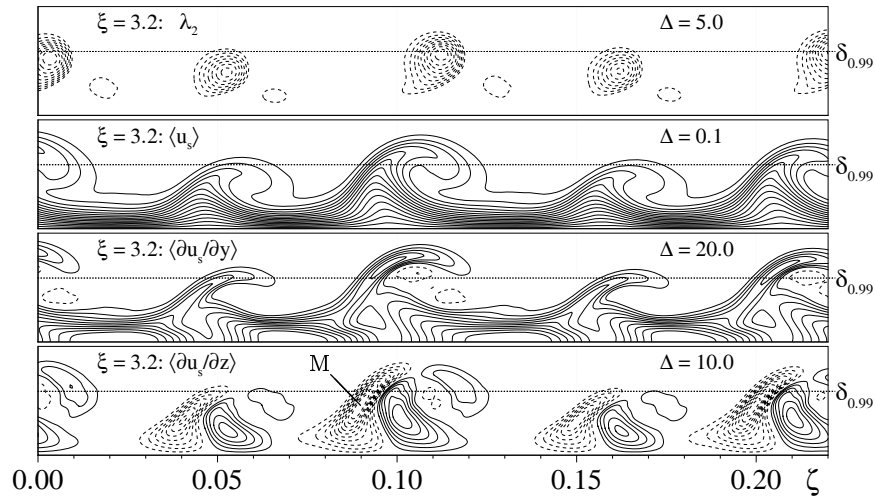


Fig. 5. Flow field distorted by the nonlinearly saturated CFV packet in a crosscut in the vortex-oriented system ($(\xi = 3.2, \zeta = 0.0) \rightarrow x = 2.487$). From top to bottom: λ_2 isolines (indicating local pressure minima, see [5]); deformed meanflow; y - and z -gradient of the deformed meanflow (negative isolines are dashed, M marks the maximum negative z -gradient). To scale.

Figure just the directional field is visualized whereas in the lower the LIC filter length is proportional to the modulus of the velocity vector and thus regions of high and low velocity can be identified by streaky or grainy patterns, respectively. The CFV cores are situated just above a layer of crosswise moving fluid, where the crossflow component of the base flow is largest (cf. the $w_{B,s}$ -profile on the right).

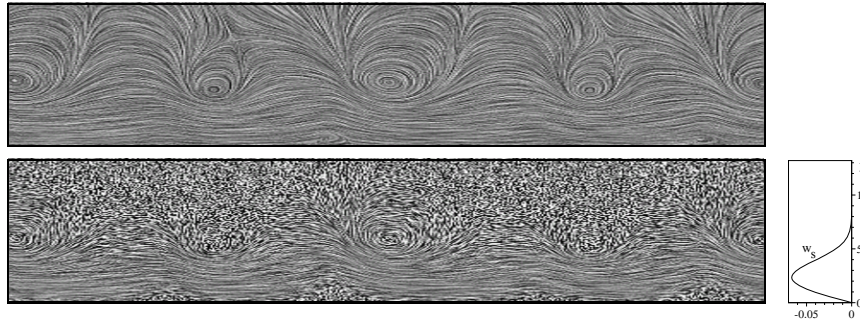


Fig. 6. Vector field (w_s, v) in a crosscut at $\xi = 3.2$ visualized by means of LIC, with (bottom) and without (top) the filter length adapted to the modulus of the velocity vector. The ζ -range corresponds to the range shown in Fig. 5. Right: Crossflow-profile $w_{B,s}$ at $\xi = 3.2, \zeta = 0.0$.

3.3 Secondary Instability

In the scenario discussed so far solely a steady disturbance input has been considered and the flow field, calculated by a high-order time-stepping scheme, finally settled to a steady nonlinear disturbance state. Naturally, transition to turbulence can only be caused by unsteady disturbances. In low turbulence freeflight conditions a sudden breakdown of the dominating CFVs is observed and the question arises, whether this phenomenon is caused by a strong convective or a global instability with respect to unsteady modes. "Global" means that a disturbance is amplified in time while remaining at a fixed finite location in space, causing inevitably a nonlinear disturbance state (example: bluff-body wake). To date there are experimental investigations (see [1] and [8]), investigations with temporal stability analysis (see [7], [13]) and a first tentative spatial DNS study (see [4]) on this issue, but all lack a definite answer whether or not the observed, sudden strong instability is of global nature as occasionally discussed. For clarification two different scenarios have been considered in the DNS investigations presented here. First, the saturated CFV packet has been combined with a low-amplitude background pulse disturbance to simulate the natural background or freestream turbulence (Case 1). Second, the combination of the CFV packet with a primary unstable, monofrequent packet of harmonic CF waves (CFW packet) of smaller amplitude (factor 1/5) within the same disturbance strip has been simulated (Case 2).

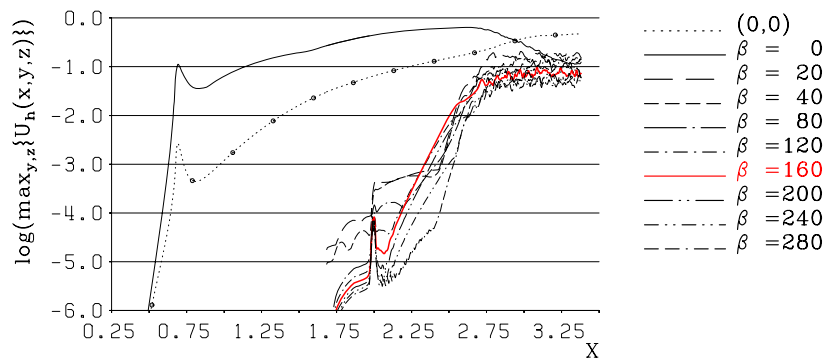


Fig. 7. Downstream t -modal amplitude development (u' -maximum over y and z) for Case 1: CFV packet plus background pulse.

First the results of Case 1 are discussed (Fig. 7), because here the underlying instability mechanism is clear-cut. The periodic background pulse, consisting of harmonic waves with frequencies from $\beta = 10$ up to $\beta = 300$

($\Delta\beta=10$), a spanwise wave number of $\gamma=\pm 90$ and an excitation amplitude of $A=5.0\cdot 10^{-5}\cdot\sqrt{Re}$ for each component, has been excited at $x=2.0$, shortly upstream of the CFV packet's saturation point. After a short transient region the background disturbances undergo a strong amplification, especially the frequency component with $\beta=160$, which attains the largest amplitude in this region. This mode grows over the smaller frequency-modes, although its receptivity is smaller. The maximum spatial amplification rate is $\alpha_i=\bar{\alpha}_i\cdot\bar{L}=\frac{1}{A}\frac{dA}{dx}\approx 6$, three times the maximum primary amplification of the most unstable CF mode. The visible growth of the low frequency as well as the higher frequency ($\beta\geq 240$) modes is clearly nonlinearly generated, noticeable just before the transition location at $x\approx 2.75$. The downstream amplification and spreading of the background wave packet in physical space is visualized by means of λ_2 -isosurfaces in Fig. 9. At $t/T=0.0$ the disturbance input is visible by the stripe pattern along $\xi\approx 2.65$. At $t/T=0.75$ a cascade of three small finger-like vortices wrapping around the left, upward moving side of the dominant CF-vortex at $\xi\approx 3.2$ emerges, with their axes aligned at 20 degrees to the CF-vortex (note the stretching of the ζ -axis). By travelling downstream an increasing number of finger-vortices appear with ongoing disturbance spreading ($t/T=0.0, 0.25$), and at this stage the corresponding but delayed development of the background disturbances on the left side of the weaker CF-vortex can be observed. The finger-vortex packets finally evolve into turbulent spots downstream of $\xi=4.0$ and merge.

Isocontours of the ($\beta=160$)- u'_s -amplitude in the crosscut corresponding to Figs. 5 and 6 (Fig. 8, top) reveal the origin of the high-frequency secondary instability. The location of the largest amplitude perfectly coincides with the largest spanwise gradient of the time averaged meanflow velocity component (Fig. 5, bottom, point M).

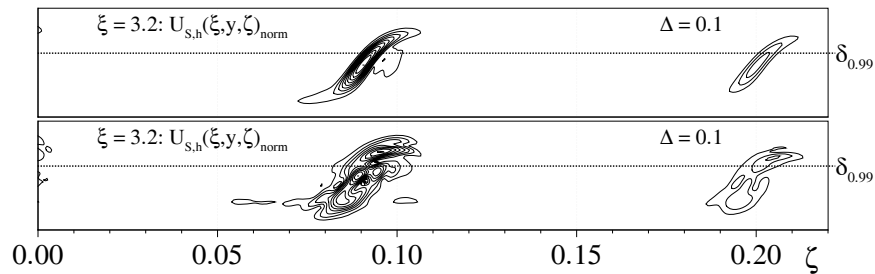


Fig. 8. Isocontours of normalized u'_s -amplitude for $\beta=160$ for Case 1 (top) and Case 2 (bottom) in the crosscut of Figs. 5 and 6.

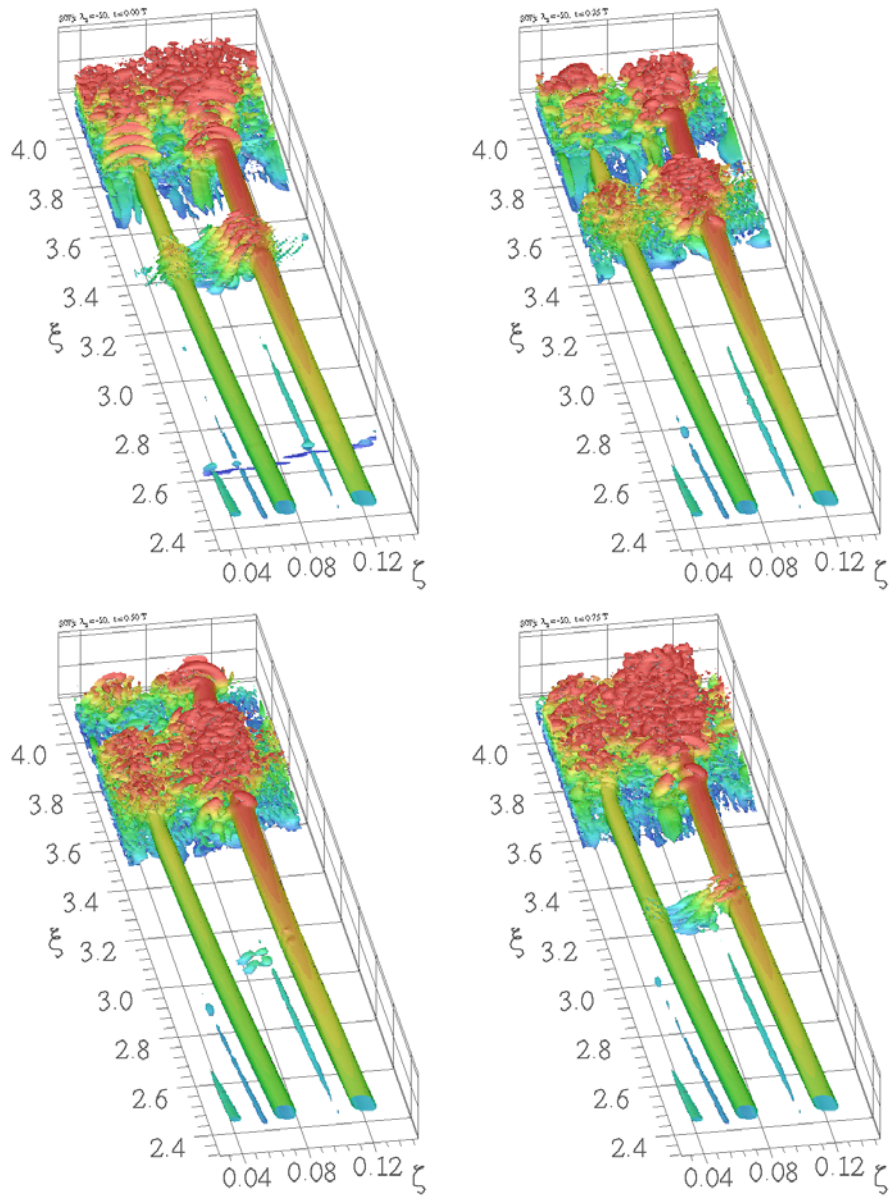


Fig. 9. Visualisation of vortical structures in the instantaneous flow fields for Case 1 (CFV packet plus background pulse) by λ_2 -isosurfaces ($\lambda_2 = -10$). From top left to bottom right: $t/T = 0.0, 0.25, 0.5, 0.75$ (T - period for $\beta = 10$). The distance from the wall is coloured from blue to red. Approximately one spanwise wavelength is shown.

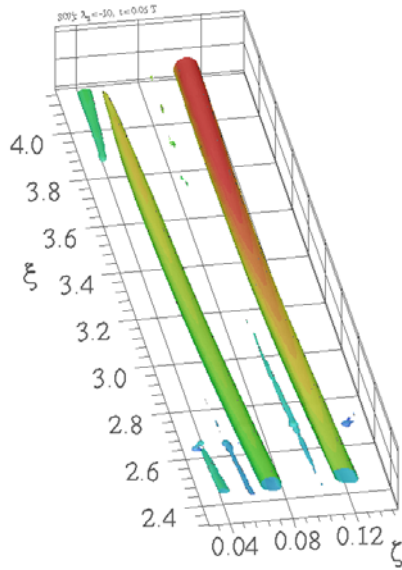


Fig. 10. Vortical structures for Case 1 at $t = t_1 + 6T$, where t_1 marks the switch-off of the background disturbance input (cf. Fig. 9).

To corroborate the convective nature of this instability mechanism, the excitation of the periodic background pulses has been switched off after some time. Then the unsteady field disturbances convect downstream and the flow field eventually relaxes fully to a steady state (Fig. 10). The convective nature could already have been anticipated from the possible time-accurate marching to the steady state with saturated CF vortices.

In Case 2 a monofrequent cross-flow wave (CFW) packet with $\beta = 20$ has been superimposed on the CFV packet, with the same spatial v' -disturbance velocity distribution within the disturbance strip, but sinusoidally varied in time. Thus the modes $(1, \pm k)$, $k=1-4$, have been added, the frequency corresponding to 1.4 times the frequency of

the integrally most amplified mode. In Fig. 11 it can be seen that the amplitudes monotonously decrease with the frequency because at first the higher frequencies are generated nonlinearly by the the fundamental modes. Thus, the secondary amplification starts at a different amplitude level compared to Case 1 and no outstandingly amplified frequency can be identified. But looking on the amplitude contourplot in Figure 8, bottom, principally the

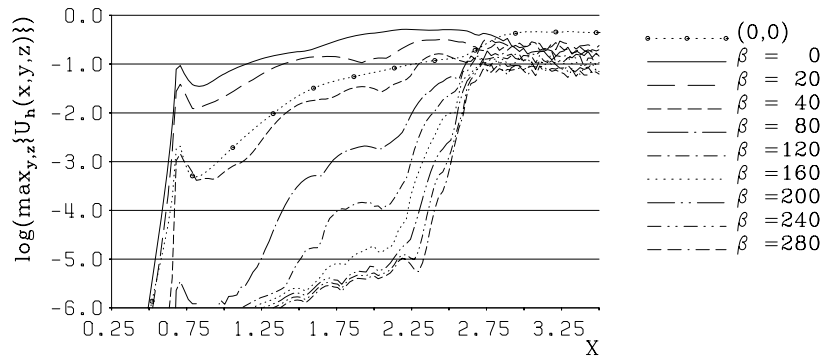


Fig. 11. Downstream t -modal amplitude development (u' -maximum over y and z) for Case 2 (CFV plus CFW packet)

same instability mechanism can be detected, with strong amplification of the disturbances on the left, up-draft side of the dominant CFV.

3.4 Transition Delay

There exist several strategies to possibly delay transition in order to reduce the skin friction of aerodynamic vehicles. One of the most elegant is trying to deform the mean flow by easy means in such a way that the disturbances triggering transition would not grow. Here the strategy of Upstream Flow Deformation (UFD) is considered by the introduction of an only weakly unstable nonlinear CF vortex with comparably small spanwise wavelength. This affects the receptivity as well as the amplification of the CFV packet and is very easy to apply in practice by attaching a regular roughness row near the leading edge of the wing. Basic experimental evidence for the working of such a method has been reported by Saric et al. [9].

In the simulation presented here (Case 3, Fig. 12) this strategy is applied to Case 2. For the UFD $\gamma = 135$ (1.5 times the wavenumber of the most amplified CFV mode), corresponding to the mode (0,3) in the CFV packet, and an excitation amplitude of 2% at $x_1 = 0.57$ has been chosen. The UFD is amplified first, generating also a large 2-D mean flow distortion, and attains a maximum physical amplitude of 34% at $x = 1.89$; thereafter it somewhat decays and at $x = 3.0$ the amplitude is 14%. Due to the dominating (0,3)-

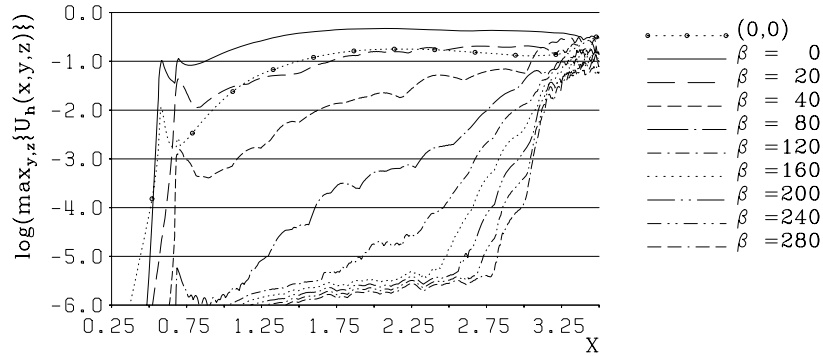


Fig. 12. Downstream t -modal amplitude development (u' -maximum over y and z) for Case 3 (Case 2 plus upstream flow deformation)

mode the maximum amplitude of the steady disturbances is higher than in Case 2, but from $x = 2.0$ the ratio turns over and thus the localized flow deceleration in Case 3 is weaker than in Case 2. The most significant result is the delay of transition indeed, which is shifted downstream to $x = 3.25$. The reason why the large amplitude UFD vortex itself does not lead to an early transition is presently under investigation.

4 Conclusions

Crossflow-instability induced laminar-turbulent transition in a swept-wing-like boundary-layer flow with decreasingly favorable chordwise pressure gradient has been investigated by spatial DNS. As a primary disturbance a packet of four steady crossflow vortex modes has been considered, modelling the effect of localized, spanwise periodic disturbances on the wing surface. The packet undergoes strong growth downstream up to amplitude saturation, and the induced strong three-dimensional deformation of the meanflow gives rise to a secondary instability with respect to high-frequency unsteady modes. It could be shown that the high-frequency disturbances can be amplified from the content of a timewise pulse disturbance or from nonlinearly generated higher harmonics of a primary unstable, low frequency disturbance. The former models natural, multi-frequency background disturbance packets, and the latter harmonic localized surface vibrations or sound/roughness effects. Secondary finger-like vortices "sliding" on the up-draft side of the primary steady vortices appear in either case, and their break-up randomizes the flow field. Most interestingly however, it could be shown for the first time in a simulation that a significant transition delay is possible in a 3-D boundary layer by a 3-D nonlinear upstream flow deformation with steady crossflow vortices of subcritical spanwise wave lengths.

Acknowledgements

The financial support by the Deutsche Forschungsgemeinschaft (DFG) within the national Schwerpunktprogramm Transition under grant KL 890/2 is gratefully acknowledged, as well as the provision of computer resources by HLRS within the project packet LAMTUR.

References

1. Bippes, H.: Environmental conditions and transition prediction in 3-D BL. AIAA-97-1906, 1997.
2. Bonfigli, G.; Kloker, M.: Spatial Navier-Stokes simulation of crossflow-induced transition in a 3-D boundary layer. In Nitsche, W.G.; Hilbig, R., (eds.): *New results in numerical and experimental fluid dynamics*. 11. STAB/DGLR Symposium, November 1998. NNFM, Vieweg Verlag, Berlin.
3. Bonfigli, G.; Kloker, M.: Three-dimensional Boundary-Layer Transition Phenomena Investigated by Spatial Direct Numerical Simulations. In Fasel, H.; Saric, W., (eds.): *Laminar-Turbulent Transition*. IUTAM Symposium Sedona, Az./USA, Springer-Verlag Berlin Heidelberg New York, 1999.
4. Högberg, M.; Henningson, D.: Secondary instability of crossflow vortices in Falkner-Skan-Cooke boundary layers. *J. Fluid Mech.* (1998), vol. 3689, pp. 339-357, United Kingdom, Cambridge University Press 1998.
5. Jeong, J.; Hussain, F.: On the Identification of a Vortex. *J. Fluid Mech.* (1995), vol. 285, pp. 69-94, 1995.

6. Kloker, M.: A robust high-resolution split-type compact FD scheme for spatial direct numerical simulation of boundary-layer transition. *Applied Scientific Research*, 59 (4), pp. 353-377. Kluwer Acad. Publishers, NL, 1998.
7. Malik, M.R.; Li, F.; Choudhari, M.M.; Chang, C-L.: Secondary instability of crossflow vortices and swept-wing boundary-layer transition. *J. Fluid Mech.* (1999), vol. 399, pp. 85-115, United Kingdom, Cambridge University Press 1999.
8. Reibert, M.S.; Saric, W.S.: Review of Swept-Wing Transition. AIAA-97-1816, 1997.
9. Saric, W.S.; Carrillo, Jr.; Reibert, M.S.: Leading-Edge Roughness as a Transition Control Mechanism. AIAA-98-0781, 1998.
10. Spalart, P.R.; Crouch, J.D.; Ng, L.L.: Numerical study of realistic perturbations in 3-D boundary layers. In *Proc. AGARD Conf.: Application of Direct and Large Eddy Simulation to Transition and Turbulence*, AGARD-CP-551, pp. 30.1 – 30.10., Chania, Crete, Greece, 1994.
11. Wassermann, P.; Kloker, M.: Direct Numerical Simulation of the Development and Control of Boundary-Layer Crossflow Vortices. In Nitsche, W.G.; Hilbig, R., (eds.): *New results in numerical and experimental fluid dynamics*. 11. STAB/DGLR Symposium, November 1998. NNFM, Vieweg Verlag, Berlin.
12. Wassermann, P.; Kloker, M.: DNS-Investigations of the Development and Control of Crossflow Vortices in a 3-D Boundary-Layer Flow. In Fasel, H.; Saric, W., (eds.): *Laminar-Turbulent Transition*. IUTAM Symposium Sedona, Az./USA, Springer-Verlag Berlin Heidelberg New York, 1999.
13. Wintergerste, T.; Kleiser, L.: Direct numerical simulation of transition in a three-dimensional boundary layer. In Henkes, R.A.W.M.; van Ingen, J.L., (eds.): *Transitional Boundary Layers in Aeronautics*. Royal Netherlands Academy of Arts and Sciences, North-Holland, Amsterdam / Oxford / New York / Tokyo, 1996.